Research Article

Amor Hedfi, Manel Ben Ali, Sirajul Haq*, Jamoliddin Razzokov, Wajid Rehman, Muhammad Waseem, Khaled Elmnasri, M. Khalid Hossain, Fazal Ur Rehman, Eldor Karimbaev, Shafia Shujaat

Effective remediation of organic pollutant using *Musa acuminata* peel extract-assisted iron oxide nanoparticles

https://doi.org/10.1515/chem-2025-0132
received August 7, 2024; accepted January 24, 2025

Abstract: The increasing environmental concerns over wastewater contamination have spurred significant interest in developing efficient and sustainable methods for wastewater treatment. In this study, a simple and user-friendly approach was employed to synthesize iron oxide nanoparticles (IO-NPs) using *Musa acuminata* peel extract as a reducing and stabilizing agent. The synthesized IO-NPs were thoroughly characterized using transmission electron microscopy, X-ray diffraction, scanning electron microscopy, Fourier-transform infrared spectroscopy, ultraviolet–visible spectroscopy, energy-dispersive X-ray spectroscopy, and thermogravimetric analysis to investigate their structural, morphological, compositional, and optical properties. The crystallite size was determined to be 38.42 nm, while the particle size was nearly double, at 65.22 nm. The IO-NPs were further evaluated for their photocatalytic efficacy in degrading methyl orange (MO) and rhodamine 6G (R-6G), two common organic dye pollutants. The highest degradation efficiency of 99.42% was achieved for R-6G, while MO showed a degradation of 79.87% within 160 min. Photocatalytic experiments were conducted under varying conditions of catalyst dosage, initial dye concentration, and solution pH to optimize the degradation process. The recycling potential of the IO-NPs was also examined by performing the photocatalytic process over five cycles, demonstrating their reusability and potential for sustainable wastewater treatment.

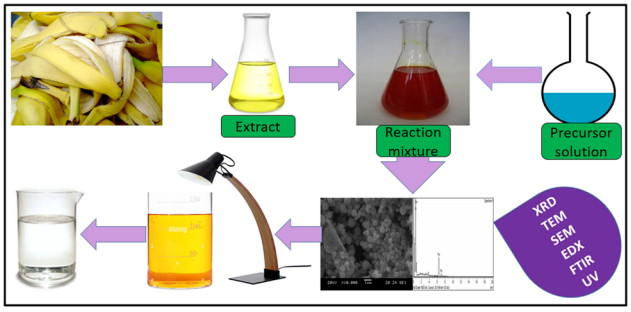

Graphical abstract

Keywords: instrumentation, iron oxide, photocatalysis, waste-water

*** Corresponding author: Sirajul Haq,** Department of Chemistry, University of Azad Jammu and Kashmir, Muzaffarabad, 13100, Pakistan, e-mail: cii_raj@yahoo.com
Amor Hedfi, Manel Ben Ali: Department of Biology, College of Sciences, Taif University, P.O. Box 11099, Taif, 21944, Saudi Arabia
Jamoliddin Razzokov: Institute of Fundamental and Applied Research, National Research University TIIAME, Kori Niyoziy 39, Tashkent, 100000, Uzbekistan; Department of Natural Sciences, Shakhrisabz State Pedagogical Institute, Shakhrisabz Street 10, Kashkadarya, 181301, Uzbekistan; Department of Biotechnology, Tashkent State Technical University, Universitet 2, Tashkent, 100095, Uzbekistan
Wajid Rehman: Department of Chemistry, Hazara University, Mansehra, KP, Pakistan
Muhammad Waseem: Department of Chemistry, COMSATS University Islamabad, Islamabad, Pakistan
Khaled Elmnasri: Laboratory of Bacteriological Research, Institute of Veterinary Research of Tunisia, University of Tunis El Manar, Tunis, 1006, Tunisia
M. Khalid Hossain: Institute of Electronics, Atomic Energy Research Establishment, Bangladesh Atomic Energy Commission, Dhaka, 1349, Bangladesh
Fazal Ur Rehman, Shafia Shujaat: Department of Chemistry, University of Azad Jammu and Kashmir, Muzaffarabad, 13100, Pakistan
Eldor Karimbaev: Institute of Fundamental and Applied Research, National Research University TIIAME, Kori Niyoziy 39, Tashkent, 100000, Uzbekistan; Department of Information Technologies, Tashkent International University of Education, Imom Bukhoriy 6, 100207, Tashkent, Uzbekistan

1 Introduction

Environmental pollution is primarily caused by the growing industrialization as well as urbanization. Water bodies, ranging from surface water to ground water resources, are found to be polluted by different pollutants, including organic dyes and several metal cations, released as a result of different

chemical and physical processes [1,2]. So, before being discharged into receiving water bodies, removal of such pollutants becomes a major concern, as these effluents are a major source of eutrophication in the ecosystem and pollution in the environment, thereby affecting both aquatic and non-aquatic life and causing damage to ecological systems [3,4]. The treatment of the contaminated industrial water serves as an important contraption against water pollution with the textile industry being a major contributor towards this issue. Almost 20% of the water contamination is attributed to the dyes that become part of the environment without ant treatment [5–7]. Among the organic dyes, methyl orange (MO) is a stable azo dye known for its environmental persistence due to its stable organic structure, making its degradation in water difficult and causing serious pollution problems. R-6G is a fluorescent dye widely used in various applications, including laser technology and biological imaging. Due to its excellent photostability and solubility in water and organic solvents, R-6G is often employed as a tracer or probe in fluorescence-based assays [8]. However, R-6G is also a synthetic organic pollutant, raising environmental concerns due to its persistence and potential toxicity [9]. Because of their assorted impacts on aquatic life and risks to human health, MO and R-6G were selected as model pollutants. These dyes use dissolved oxygen in water during chemical or biological decomposition and release toxic byproducts [10]. Conventional methods, including flocculation, membrane filtration, coagulation, and adsorption, manipulate toxic chemicals and result in the partial removal of dyes [11,12]. Besides these methods, photocatalysis is a low-cost, simple chemical process catalyzed by solids in the presence of suitable external radiation with wavelengths in the ultraviolet (UV) and visibleregions [13]. In this process, solar energy is utilized for energy production and environmental purification. It is advantageous over other purification techniques in terms of efficient decomposition of different classes of pollutants and the formation of no polycyclic byproduct. The use of solid catalysts speeds up the reaction under light irradiation by generating electron–hole pairs, which enable the chemical transformation of reactants and regenerate their chemical composition [14,15].

Recently, several types of decontaminants have been employed for wastewater treatment, with natural sources such as biochars being utilized to remove both organic and inorganic pollutants [16,17]. However, among the materials utilized, metal, metal oxide, and metal sulfide NPs have attained much attention from researchers due to their preeminent applications, including sensing, energy storage, antimicrobial and anticancer activities, catalysis, supercapacitors, tumor detection, and wastewater treatment [18–23]. Among metal oxides, iron oxide nanoparticles (IO-NPs) are highly stable and have a lower band gap of 2.2–2.3 eV that allows them to absorb light from the visible range and thereby eliminate reliance on the UV spectrum for photocatalysis [22]. The IO-NPs are widely used as photocatalysts because of their significant optical properties, nontoxic nature, chemical stability, as well as ease of recovery from the reaction medium [24,25]. Nanoparticles of IO are easy to prepare and are widely used for environmental and biomedical applications [26–28]. For preparing IO-NPs, various synthetic methods have been documented, which include chemical vapor deposition, sol–gel, pyrolysis, hydrothermal, as well as chemical precipitation [15]. These techniques call for wide utilization of toxic reagents in addition to high temperature and pressure. Plant-mediated synthesis of NPs, an efficient alternative way for synthesizing IO-NPs, has drawn the attention of researchers. Plant-mediated fabrication is an easy, economical, and ecofriendly way for nanoparticle synthesis [29–31]. Due to its environmentally friendly and economical nature, plant-mediated synthesis has gained significant attention, and a lot of research has been conducted on preparing nanomaterials using plant extract, including peppers, lemon peels, *Justicia adhatoda,* and *Pedanum harmala* [32–36]. Rosli et al. synthesized IO-NPs using ferric sulfate heptahydrate and *Averrhoa bilimbi Linn* extract, which were characterized via Fourier-transform infrared (FTIR) and UV–visible spectroscopies, and their antioxidant activity against DPPH free radicals was studied [37]. Likewise, Haris et al. prepared IO-NPs through *Oscillatoria limnetica* extract, and their antibacterial, antifungal, antioxidant, hemolytic, and brine shrimp cytotoxicity activities were performed [38]. On plant-assisted fabrication of IO-NPs, even though there have been a number of published articles, only one article focuses on using banana peel extract for the preparation of Fe_3O_4 NPs with investigations limited to their magnetic properties only [39]. This research work also focuses on the preparation of *M. acuminata* peel extract for IO-NPs, but the procedure used for preparing the extract is quite different from those reported in the literature. This is a single-pot, low-temperature process that eliminates the need for hazardous chemicals, complex equipment, or energy-intensive procedures, making it simple, cost-effective, and accessible for broader adoption. This approach not only minimizes environmental pollution associated with chemical synthesis but also promotes waste valorization. Moreover, the peel of *M. acuminate* is an abundant agricultural waste product rich in bioactive substances like antioxidants, flavonoids, and polyphenols [40]. These substances serve as organic stabilizing as well as reducing agents, which makes peel extract a great candidate for ecofriendly NPs fabrication. A comprehensive physicochemical study using different available techniques also distinguishes this research work from the reported data. Furthermore,

NPs of IO mediated by *M. acuminata* peel extract are never employed for MO photodegradation. This also demonstrates the reusability of the IO-NPs over multiple cycles without losing the catalytic property.

The current research work reports the fabrication of IO-NPs using *M. acuminata* peel extract manipulated for the photocatalytic degradation of MO. The prepared IO-NPs were characterized via energy-dispersive X-ray (EDX), scanning electron microscopy (SEM), transmission electron microscopy (TEM), DRS, X-ray diffraction (XRD), and FTIR spectroscopy. During the photocatalytic reaction, a UV–visible spectrophotometer was employed to track the decline in the absorbance maxima of MO. It was also observed that how the photocatalytic process was affected by pH, temperature, catalyst dosage, and starting concentration.

2 Research methodology

2.1 Reagents used

In this research work, reagents used were analytical -grade and were bought from Sigma-Aldrich (St. Louis, MO, USA). These reagents included ferric sulfate heptahydrate (99%) and MO (98%) and were utilized without any further purification. To wash the glass labware, a 15% HNO_3 solution was employed, followed by distilled water (DW). The solutions required for different reactions were prepared in DW.

2.2 Extract preparation

The extract was prepared from the collected waste *M. acuminata* peels following a standard procedure with minor modifications [41]. The collected waste *M. acuminata* peels were cut down into small pieces of about 1.5 cm and washed twice using ordinary water, then the DW. To remove surface moisture, washed peels were wrapped in a clean filter paper and then stored in an airtight thermos bottle. At 80°C, 500 mL DW was boiled and transferred into the thermos bottle containing the clean waste *M. acuminata* peels. Light yellow-colored crude extract was obtained after 2 h, which was filtered twice with Whatmann filter paper [40] and later stored at 4°C in an airtight flask.

2.3 Fabrication of IO-NPs

After dissolving 2.07 mg of $FeSO_4{\cdot}7H_2O$ in 500 mL DW to create the standard solution (15 mM), 70 mL of stock solution was put into a conical flask with 30 mL of produced extract. Brick-red precipitate appeared after 45 min of stirring the reaction mixture at 250 rpm and 50°C. The aging process of the precipitate was continued for 6 h followed by filtration and subsequent washing process with hot DW thrice to remove any uncoordinated ions. The sample was stored in a glass bottle and oven-dried at 140°C after being filtered.

2.4 Characterization

The Panalytical X'pert Pro (manufactured in CA, USA) was used for the crystallographic analysis. It was operated at 30 mA as well as 40 kV, with a scanning speed of 5 min^{-1} per 2θ. The microstructure of IO-NPs was investigated using the SEM model JEOL 5910 (Tokyo, Japan) and the TEM model Hitachi HT7800 (Cleveland, TN, USA). In contrast, elemental analysis was carried out using EDX (INCA 200) (Oxfordshire, UK) in conjunction with SEM. A known quantity of IO-NPs was heated to 1,000°C with a 10°C rise per minute using the Perkin Elmer model 6300 thermogravimetric analysis analyzer to record the thermogram. Optical characteristics were studied using the Shimadzu UV-800 Pharmaspec spectrophotometer, and the Tauc plot was used to compute the band gap energy. Utilizing KBr pellets, the chemical composition was investigated using an FTIR Nicolet 670 in the 4,000–400 cm^{-1} range. Thermo Fisher Scientific Waltham, MA, USA, supplied the FTIR and UV–visible spectrophotometers [42–44].

2.5 Photocatalytic assay

In the presence of IO-NPs, a 15 mM solution of MO and R-6G was degraded throughout the photo-induced reaction, which was performed under simulated solar light. To establish sorption desorption steadiness, the reaction, which involved 50 mL of stock solution and 20 mg of IO-NPs, was agitated for 45 min without light. Following the reaction mixture's exposure to artificial sunlight, 3 mL was spectrophotometrically examined after a predetermined amount of time, and the absorbance peak's drop with the passage of time was recorded. The percentage degradation and degradation rate constant were calculated using mathematical equations (equations (1) and (2)), where C_o is the initial concentration and C_t is the final concentration. Under the same reaction conditions, the impact of catalyst dosage, initial concentration, and pH on MO degradation was also assessed

$$\% \text{ Degradation} = \frac{C_o - C_t}{C_o} \times 100, \quad (1)$$

$$\ln\left(\frac{C_t}{C_o}\right) = -kt. \quad (2)$$

3 Results and discussion

3.1 Physicochemical study

To investigate the crystalline nature of IO-NPs and extract additional crystallographic characteristics from the XRD data, an XRD analysis was performed (Figure 1). The shape of the diffractogram was a bit noisy, which suggested that the sample may possess some amorphous content along with a crystalline phase. Similar observations have also been studied previously during the synthesis of SnO_2 NPs [42]. The diffractogram shown in Figure 2 exhibited characteristic diffraction peaks assigned to different crystallographic planes of the IO-NPs that were mentioned in the XRD pattern above corresponding reflections. In accordance with the JCPDS card 01-071-4918 and the corresponding miller planes, diffraction peaks at the 2-theta position were identified. On the basis of the available information provided in the JCPDS card, the Fe_2O_3 crystallites were formed with a cubic geometrical shape, where lengths of all three coordinates (*a*, *b*, and *c*) were 4.582 Å with an interfacial angle of 90° between the coordinates. The average crystallite size, calculated from the XRD data, was 38.42 nm, with a lattice strain of 0.149%.

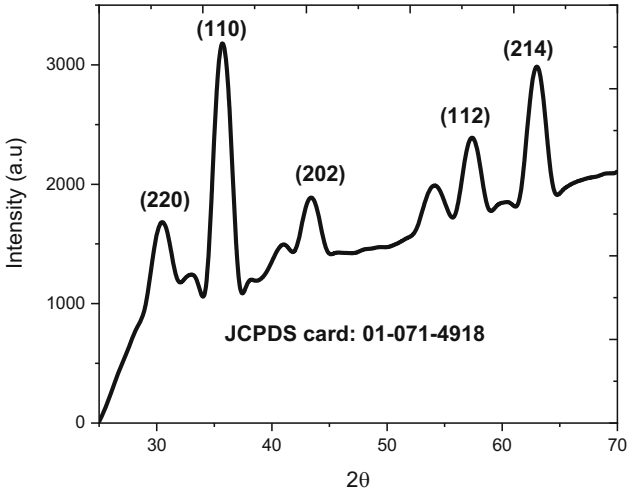

Figure 1: XRD pattern of IO-NPs.

To examine the morphology of prepared IO-NPs, SEM analysis was performed. Figure 2 displays obtained low and high micrographs that were synthesized. In low magnification image (a), most of the particles seemed to be round or nearly round in shape and were irregularly distributed. The lower left portion of the image (a) was seen to be slightly agglomerated, forming larger particles, whereas small particles resided upon the surface of the larger ones. In high magnification image (b), three perfect spherical particles were seen, whereas several nearly spherical-shaped particles were present. The spherical particles exhibited well-defined boundaries, whereas the nearly spherical particles seemed to be fused with one another; however, their fusion did not lead to the formation of larger agglomerates. It has been reported in the literature that because of the high surface energy, the particles tend to fuse together [45].

TEM analysis was performed to have a better understanding of the morphology of IO-NPs, and the resulting micrograph is presented as Figure 3. The TEM image showed that the particle exhibited a nearly spherical

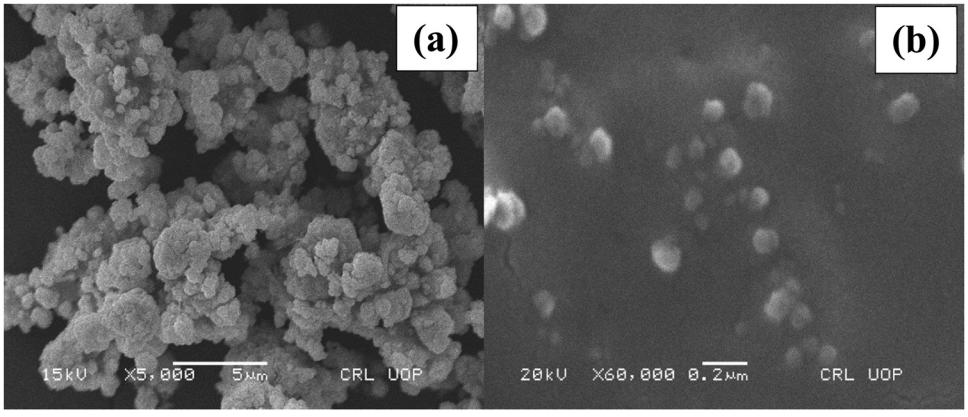

Figure 2: Low (a) and high (b) magnification SEM micrographs of IO-NPs.

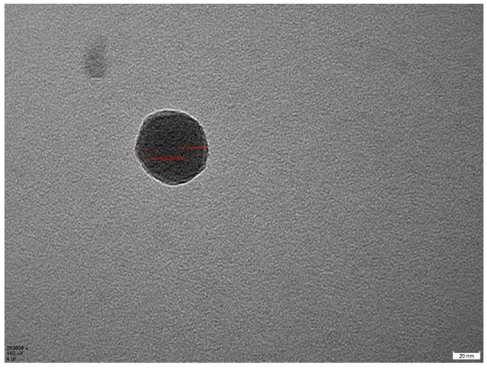

Figure 3: TEM micrographs of IO-NPs.

morphology. Upon close observation, it was observed that the particle had a porous surface. The particle size was found to be 56.22 nm.

Using EDX coupled with SEM, IO-NPs' elemental composition was assessed, and the obtained EDX spectrum is shown in Figure 4. The presence of carbon, which may have resulted from the use of carbon tape for sample streaking during EDX analysis, was the cause of the band at 0.4 keV. Three peaks in the EDX spectrum at 0.6, 6.40, and 7.12 keV confirmed the presence of iron in the sample. The existence of oxygen in the sample was ascribed to a sharp signal at 0.50 keV, which confirmed the formation of iron oxide. The detected weight% of iron and oxygen in the sample were 78.21 and 21.79, respectively.

A two-stage weight loss was seen in the thermogram of IO-NPs shown in Figure 5. The first weight loss, detected between 48 and 130°C, was because of the evaporation of moisture and physisorbed water, with a total of 9.71% (0.68 mg) weight loss in this stage. Approximately 12.02% of the weight (0.76 mg) was lost during the second weight loss, which occurred between 220 and 535°C and was caused by the loss of chemisorbed water [46].

The chemical moieties in the IO-NPs were analyzed through FTIR, and the resultant spectrum is presented in

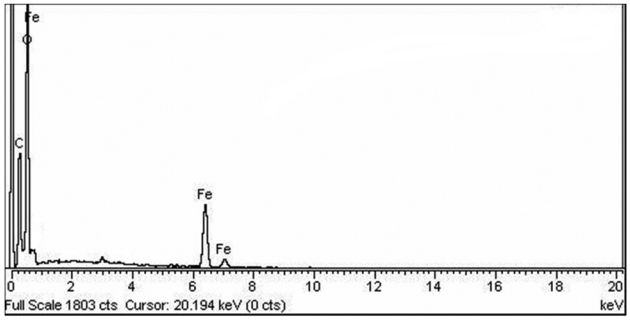

Figure 4: EDX spectrum of IO-NPs.

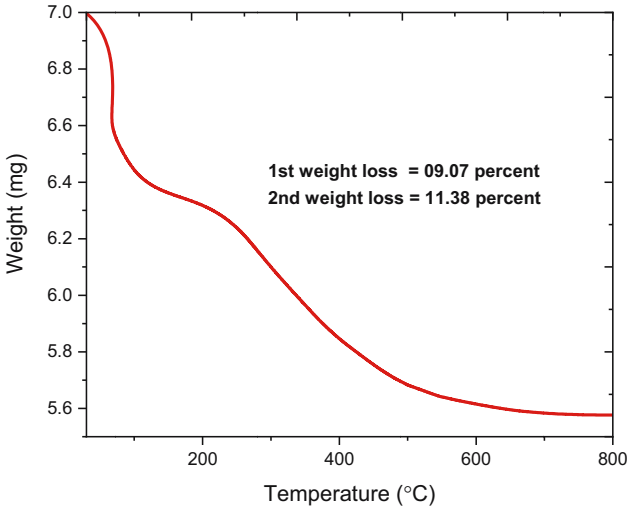

Figure 5: Thermogram of IO-NPs showing weight loss in two stages.

Figure 6, where most of the bands corresponded to the existence of the hydroxyl group as well as Fe–O stretching. The non-bonding water molecules were responsible for the short band at 3742.51 cm^{-1}, while the stretching vibration of –O–H and the band for bending vibrations at 1639.28 cm^{-1} were represented by the wide wave band in the 3394.72–3038.59 cm^{-1} range [43,47,48]. The bands at 1054.72, 755.63, and 726.76 cm^{-1} were indicative of metal–oxygen (M–O) stretching and bending vibrations within the iron hydroxide structure, respectively [49,50]. The bands at 473.90 and 435.24 cm^{-1} could correspond to lattice vibrations involving iron–oxygen bonds [51]. The FTIR results suggested the formation of pure IO-NPs with no impurities.

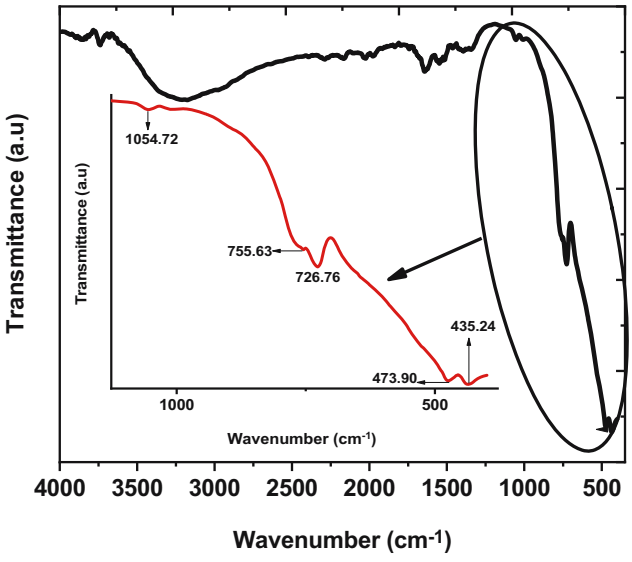

Figure 6: FTIR spectrum of IO-NPs.

A strong absorbance band at 312.35 nm in the UV–visible spectra of IO-NPs is depicted in Figure 7 and was associated with an electronic transition known as a "direct band-to-band transition." The energy level at which electrons in the nanoparticles are shifted from VB to CB was correlated with this transition. Tauc's plot indicated that the band gap energy was 3.20 eV. The least amount of energy needed to transfer an electron from VB, which is the highest energy level where electrons live, to CB, which is the lowest energy level where electrons can freely migrate, is known as the band gap energy. The energy of photons having a wavelength of 312.35 nm was equal to this energy. The IO-NPs' wide range of applications was indicated by their band gap energy of 3.20 eV. By absorbing photons with a wavelength of 312.35 nm, the VB electrons gained sufficient energy to move to the CB, enabling effective charge transport and the creation of electron–hole pairs, that can play a key role in the photocatalytic process.

3.2 Photocatalytic study

Photocatalytic efficacy of IO-NPs fabricated via the biological method was inspected under full light spectrum against the degradation of MO, and Figure 8 displays the findings. First, DW was used to create the dye's stock solution, and 50 mL of this solution was added to the vessel containing the catalyst. The reaction mixture was stirred for 30 min without light in order to achieve the sorption and release steadiness of the dye molecule. It was then analyzed using a UV–visible spectrometer, and it was found that at 464 nm, the highest absorption took place. Following the observation of the liquid samples at predetermined intervals of 10, 20, 40, 80, 120, and 160 min, the decrease in the absorbance maxima was noted as a function of time. The solution became colorless after 160 min, suggesting that all of the dye had been degraded. With a degradation rate of 0.00873 per min, the percentage degradation in the same time period was 79.87%. The photocatalytic efficiency of IO-NPs was also tested against the rhodamine 6G dye under the same reaction conditions as discussed above, and the obtained results are revealed in Figure 9(a–d). The degradation profile (Figure 9(a)) at 526 nm exhibited a gradual decline in the absorbance maxima over time, suggesting the degradation of chromophore responsible for the absorption of light at 526 nm. The percentage degradation plot (Figure 9(c)) showed that percentage degradation increased with the passage of time, and after 160 min, 99.42% of R-6G was degraded. The degradation rate constant was determined by applying equation (2), where the result displayed 99.42% of R-6G with a degradation rate of 0.03012 per min. When IO-NPs photocatalyzed the degradation of both dyes, they excited valance electrons with light energy equal to the catalyst's band gap energy, forming reactive species such as superoxide radicals, hydroxyl radicals, and positive holes [52]. After interacting with the adsorbed dye molecules on the IO-NPs' surface, these reactive species started a series of oxidation processes that degraded the pollutant into less dangerous and simpler forms. IO-NPs' distinct electrical and surface characteristics were essential to the photocatalytic process, which made them efficient catalysts for the photo-degradation of organic pollutants [53,54].

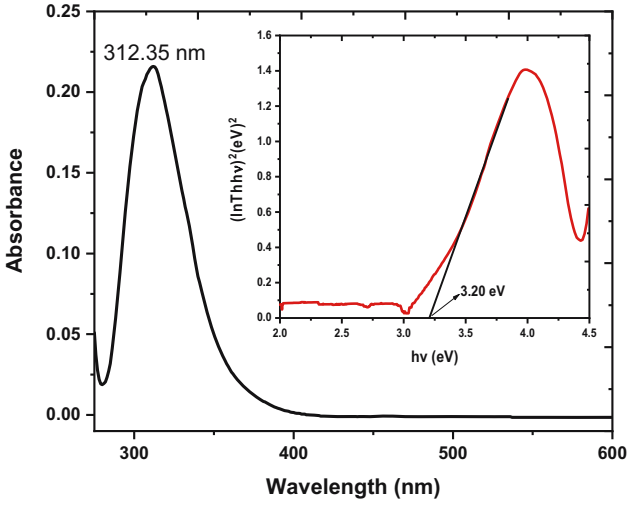

Figure 7: UV–visible spectrum (inset: Tauc's plot) of IO-NPs.

The absorption of photons with energies higher than the semiconductor's band gap started a sequence of intricate processes that led to the photocatalytic degradation of MO in the presence of IO-NPs. Electrons were stimulated from the IO-NPs' VB to the CB upon photon absorption, leaving holes in the VB behind. These photogenerated electron–hole pairs have the ability to get to the NP's surface and engage in redox reactions with substances that have been adsorbed. Superoxide radicals (O_2^-) can be created when the electrons combine with adsorbed oxygen, while hydroxyl radicals ($^{\cdot}OH$) can be produced when the holes react with water molecules. Superoxide and hydroxyl radicals are both extremely reactive substances that have the ability to oxidize organic color molecules, causing them to break down into less hazardous, simpler substances like CO_2 and H_2O [55,56].

3.2.1 Impact of pH

The percent photodegradation of MO in the photocatalytic reaction was observed for pH values ranging from 4 to 9

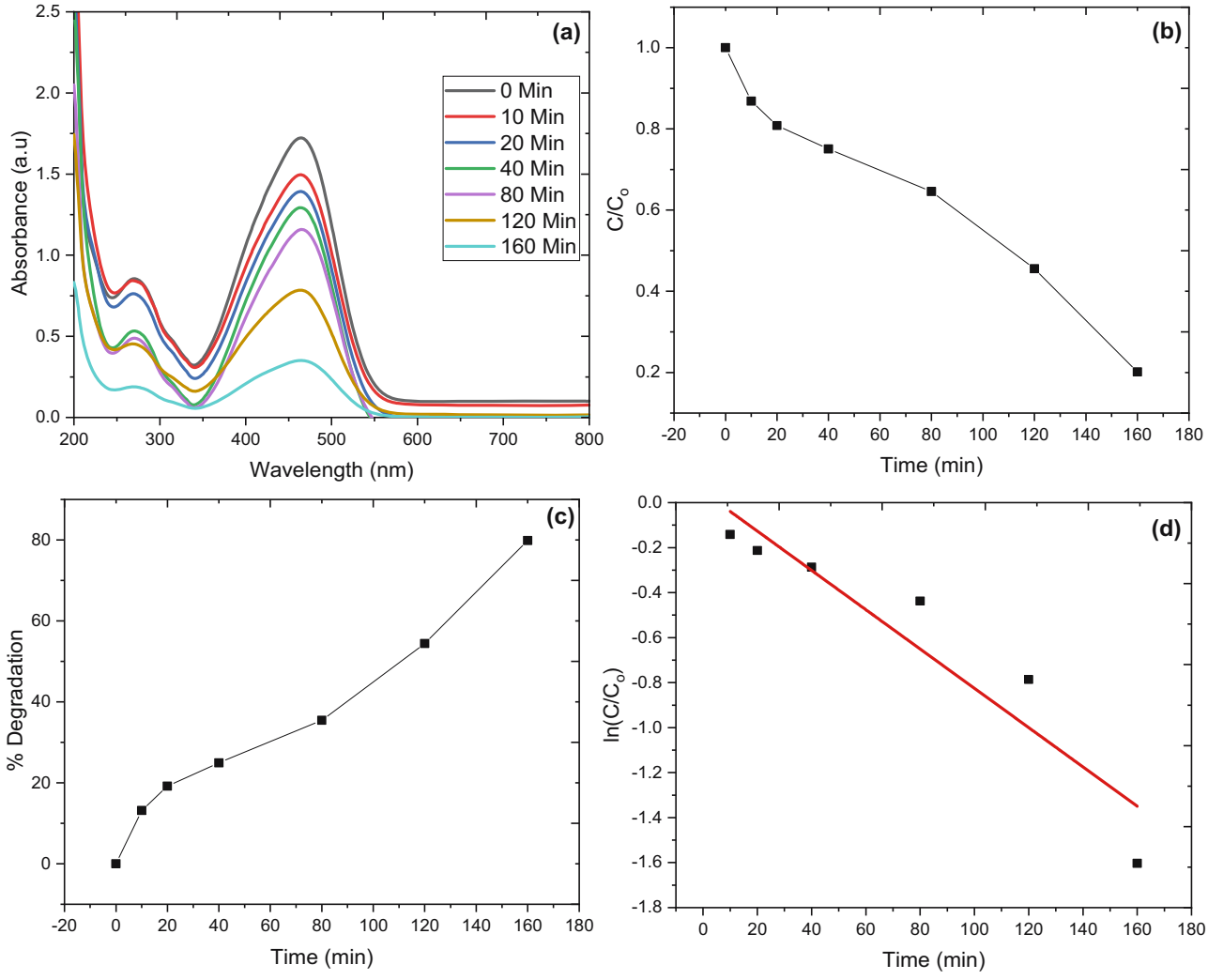

Figure 8: (a–d) Photocatalytic data of the MO degradation in the presence of IO-NPs under simulated solar light.

while allowing the remaining reaction under constant conditions (Figure 10(a)). The results demonstrate that the pH also affected the rate of photocatalytic effects. Against 20 mg IO-NPs and 15 ppm MO solution, the pH effect was examined. Recorded results exhibited that maximum degradation occurred at pH 6 [57].

3.2.2 Effect of dose

Various quantities of the IO-NPs viz. 5, 10, 15, 20, 25, and 30 mg were manipulated against the mineralization of the MO. Findings indicated that the degradation rate increased correspondingly with increasing catalyst's dose and was maximum at 20 mg, but the further increment in catalyst's quantity decreased the degradation rate. It can be explained by the catalyst's surface not having any active sites [58,59].

3.2.3 Effect of initial concentration

To examine the photocatalytic activity, IO-NPs were exposed to 5, 10, 15, 20, 25, and 30 ppm of the dye solution (MO) in this study. The findings showed that the photocatalytic activity was significantly influenced by the initial concentration. Initially, activity increased upon increasing initial concentration and was found to be maximum at 15 ppm, but then there was a gradual decrease on increasing initial concentration. The main reason behind this decrease was the blockage of light penetration due to the dye molecules, which at first interacted with the catalyst but later started

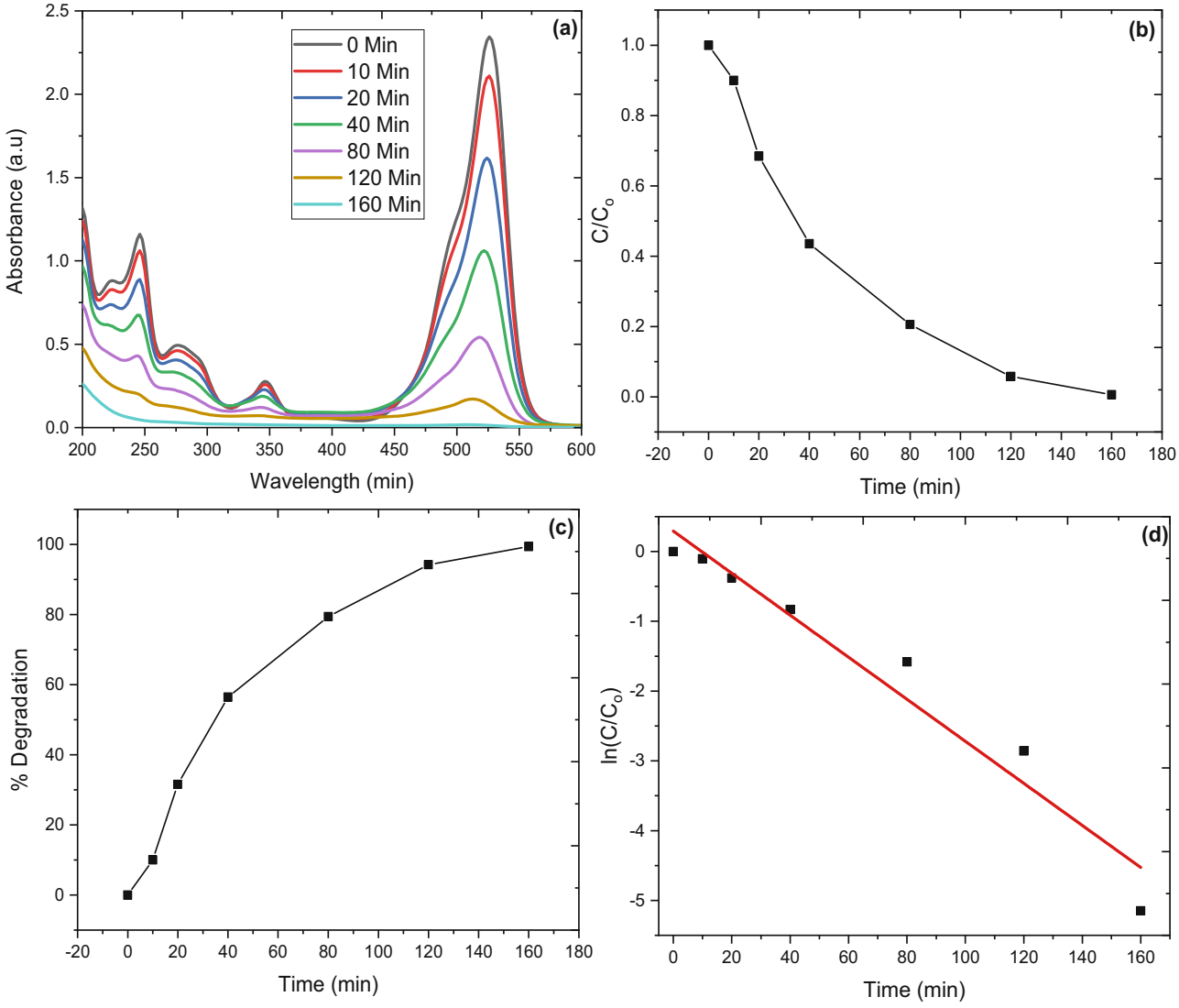

Figure 9: (a–d) Photocatalytic data of the R-6G degradation in the presence of IO-NPs under simulated solar light.

accumulating in the solution, thus reducing the photocatalytic efficacy [57,60].

3.2.4 Reuse of catalyst

An important aspect of the photocatalytic investigation was the reusability of the IO-NPs as catalysts. In this study, the photocatalytic degradation experiments were conducted over five successive cycles. It was observed that the percent degradation of MO gradually decreased over five cycles from an initial value of 79.87%, reduced to 77.73, 68.94, 53.83%, and finally 38.65% (Figure 10(d)). This trend highlighted the diminishing efficiency of the catalyst upon multiple usages. The decline in the degradation efficiency of IO-NPs with successive cycles underscored the necessity of catalyst regeneration or replacement. The decreasing efficiency can be attributed to the catalyst surface fouling, aggregation, and potential degradation of active sites [61,62].

3.3 Discussion

The physicochemical analysis revealed the synthesis of crystalline IO-NPs with nearly spherical shape, which were extremely pure, as evidenced by the XRD, TEM, EDX, and FTIR results. The crystallinity reduced structural defects, which enhanced the production of reactive species like superoxide anions as well as hydroxyl radicals necessary for dye degradation and also minimized charge recombination. The ordered crystal structure made the nanoparticles less susceptible to the degradation process, which enhanced

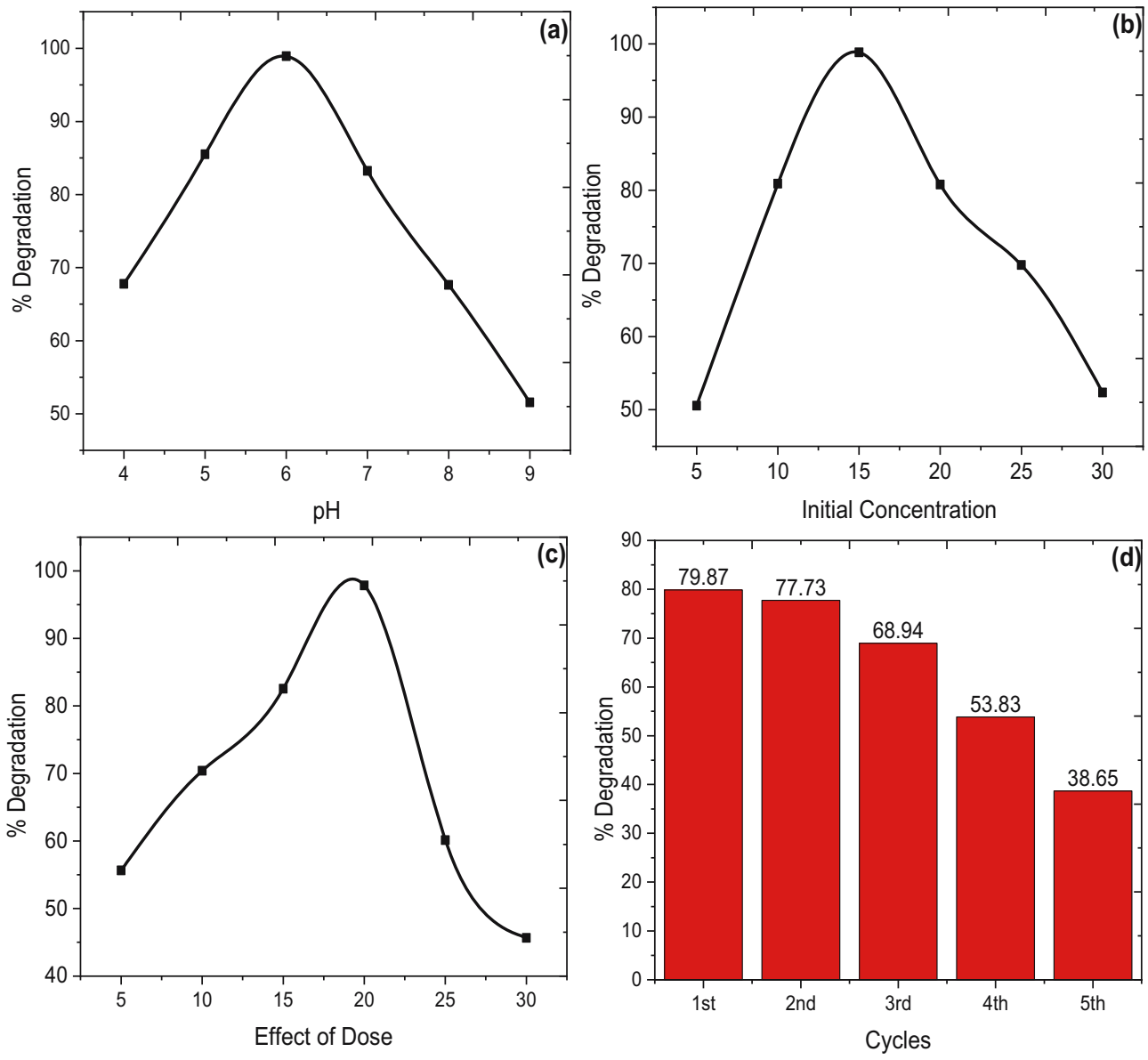

Figure 10: (a–d) Effect of pH (a), effect of initial concentration (b), effect of dose (c), and reuse efficacy of the IO-NPs during the photocatalytic experiment.

Table 1: Comparative analysis of the photocatalytic potential of the IO-NPs reported in the literature

Sources/method	Dye	Dye concentration	Catalyst dose	Contact time	Percentage degradation (%)	References
Carica papaya	Yellow RR	70 ppm	0.8 g/L	6 h	76.6	[15]
Sol–gel	Congo red	100 g/L	50 g	1 h	60	[63]
Purpureocillium lilacinum	Navy blue Safranin	100 ppm	—	2 h	49.3 66	[64]
Aspergillus carbonarious	Tanning wastewater	unknown	50 g	24 h	28	[64]
M. acuminata	MO Rhodamine 6G	15 mM	20 mg	2.40 h	79.87 99.42	Current study

their durability in reaction. As far as the morphology of the NPs was concerned, the nearly spherical shape provided a larger surface area for adsorbing dye molecules and light harvesting, facilitating more efficient catalytic reactions. Moreover, the nearly spherical shape promoted uniform dispersion in aqueous solutions, reducing diffusion resistance, and allowing faster access of dye molecules to active sites. It also ensured the uniform light absorption phenomenon and effective utilization of light energy across the NPs' surface. Likewise, the thermal stability also ensured robustness under prolonged light irradiation, maintaining consistent photocatalytic performance over time. The band gap energy is needed for the excitation of an electron from VB to CB. Low band gap energy, in this context, makes it possible to use solar light to excite electrons and initiate the photocatalytic reaction. Reactive oxygen species (ROS), such as superoxide anions and hydroxyl radicals, are produced in greater quantities during photocatalytic reactions involving lower-energy photons. These ROS are essential for the degradation of dye molecules.

3.4 Comparative analysis

The photocatalytic efficacy of the IO-NPs synthesized in this study was evaluated as well as contrasted with similar studies documented in the literature, as summarized in Table 1. The tabulated data highlighted key information, including the sources and methods employed for the production of IO-NPs in various studies, along with the experimental conditions under which their photocatalytic activity was assessed. A detailed analysis of the data revealed that the IO-NPs produced in this study demonstrated superior photocatalytic potential compared to those reported in previous works. This conclusion was substantiated by the significantly higher percentage of dye degradation achieved under comparable experimental conditions. The enhanced performance of the IO-NPs synthesized in this study highlighted the effectiveness of the adopted synthesis method and experimental design, making these nanoparticles an extremely effective photocatalyst for applications including environmental remediation applications.

4 Conclusion

The results demonstrated that the IO-NPs were successfully synthesized via an eco-friendly way and exhibited promising photocatalytic activity under visible light for the degradation of MO. The synthesis of crystalline iron oxide phases was validated by XRD analysis, while the nearly spherical morphology of IO-NPs was revealed by TEM images. FTIR and EDX analyses provided insights into the functional groups and elemental composition, respectively. UV–visible spectroscopy indicated nanoparticles' ability to absorb visible light, a crucial factor for effective photocatalysis. Study's findings underscored the potential of utilizing naturally derived precursors for the green synthesis of effective photocatalytic materials. The recyclability of the IO-NPs further highlighted their practical applicability for multiple wastewater treatment cycles. As a whole, for wastewater treatment, this study contributed in developing sustainable as well as efficient photocatalytic materials, aligned with contemporary efforts for green and cost-effective environmental remediation strategies.

Acknowledgments: The authors extend their appreciation to Taif University, Saudi Arabia, for supporting this work through project number (TU-DSPP-2024-158).

Funding information: The research was financially supported by Taif University, Saudi Arabia, for supporting this work through project number (TU-DSPP-2024-158).

Author contributions: Amor Hedfi and Manel Ben Ali – Formal analysis, visualization and funding acquisition; Sirajul Haq (Supervision), Wajid Rehman, Muhammad Waseem, Jamoliddin Razzokov – Conceptualization, methodology and project administration; Shafia Shujaat – writing – original draft; Khaled Elmnasri, M. Khalid Hossain – Software and Data curation; Eldor Karimbaev and Fazal Ur Rehman – Validation and Writing – review & editing.

Conflict of interest: It has been declared that there is no conflict of interest associated with this manuscript.

Ethical approval: The conducted research is not related to either human or animals use.

Data availability statement: The datasets generated during and/or analysed during the current study are available from the corresponding author on reasonable request.

References

[1] Jasmine J, Ponvel KM. Synthesis of Ag_2CdS_2/carbon nanocomposites for effective solar–driven dye photodegradation and electrochemical application. ES Energy Env. 2023;20:1–15.

[2] Kumar SA, Singh MV, Bhatt N, Jayaswal P, Sethi M, Burcar E, et al. The perils of heavy metal contamination in groundwater: impacts on human health in the northeastern region of Jhunjhunu, Rajasthan. ES Food Agrofor. 2024;16:1–9.
[3] Lu L, Ma Y, Liu H, Dong R, Tan P, Yang L, et al. Controlled preparation of hollow Zn0.3Cd0.7S nanospheres modified by NiS1.97 nanosheets for superior photocatalytic hydrogen production. J Colloid Interface Sci. 2022 Jan;606:1–9.
[4] Zhang H, Wang Z, Zhao Y, Cui W, Zhang X, Wang S, et al. Metal ion (Cr^{3+}, Eu^{3+}, UO^{22+}) adsorption on gibbsite nanoplates. Eng Sci. 2023;24:896.
[5] Chiou JR, Lai BH, Hsu KC, Chen DH. One-pot green synthesis of silver/iron oxide composite nanoparticles for 4-nitrophenol reduction. J Hazard Mater. 2013;248–249(2):394–400. doi: 10.1016/j.jhazmat.2013.01.030.
[6] Cheng M, Yao C, Su Y, Liu J, Xu L, Bu J, et al. Cyclodextrin modified graphene membrane for highly selective adsorption of organic dyes and copper(II) ions. Eng Sci. 2022;18:299–307.
[7] Zhang H, Ding X, Wang S, Huang Y, Zeng XF, Maganti S, et al. Heavy metal removal from wastewater by a polypyrrolederived N-doped carbon nanotube decorated with fish scale-like molybdenum disulfide nanosheets. Eng Sci. 2022;18:320–8.
[8] Shoukat S, Haq S, Rehman W, Waseem M, Hafeez M, Din SU, et al. Remediation of chromium (VI) and rhodamine 6G via mixed phase nickel-zinc nanocomposite: synthesis and characterization. J Inorg Organomet Polym Mater. 2021;31(4):1565–75. doi: 10.1007/s10904-020-01776-3.
[9] Haq S, Rehman W, Waseem M, Meynen V, Awan SU, Khan AR, et al. Effect of annealing temperature on structural phase transformations and band gap reduction for photocatalytic activity of mesopores TiO_2 nanocatalysts. J Inorg Organomet Polym Mater. 2021;31(3):1312–22.
[10] Kazazi M, Moradi B, Delshad Chermahini M. Enhanced photocatalytic degradation of methyl orange using Ag/Sn-doped CeO_2 nanocomposite. J Mater Sci Mater Electron. 2019;30(6):6116–26. doi: 10.1007/s10854-019-00913-0.
[11] Wang Y, Hu K, Yang Z, Ye C, Li X, Yan K. Facile synthesis of porous ZnO nanoparticles efficient for photocatalytic degradation of biomass-derived bisphenol a under simulated sunlight irradiation. Front Bioeng Biotechnol. 2021;8:1–11.
[12] Hunge YM, Yadav AA, Kang SW, Kim H. Photocatalytic degradation of tetracycline antibiotics using hydrothermally synthesized two-dimensional molybdenum disulfide/titanium dioxide composites. J Colloid Interface Sci. 2022 Jan;606:454–63.
[13] Długosz O, Szostak K, Banach M. Photocatalytic properties of zirconium oxide–zinc oxide nanoparticles synthesised using microwave irradiation. Appl Nanosci. 2020;10(3):941–54. doi: 10.1007/s13204-019-01158-3.
[14] Yadav AA, Hunge YM, Kang SW. Porous nanoplate-like tungsten trioxide/reduced graphene oxide catalyst for sonocatalytic degradation and photocatalytic hydrogen production Keywords: Multifunctional WO_3/rGO Photocatalytic H_2 production Sonocatalytic degradation. Surf Interfaces. 2021;24:101075. doi: 10.1016/j.surfin.2021.101075.
[15] Bhuiyan MSH, Miah MY, Paul SC, Aka TD, Saha O, Rahaman MM, et al. Green synthesis of iron oxide nanoparticle using Carica papaya leaf extract: application for photocatalytic degradation of remazol yellow RR dye and antibacterial activity. Heliyon. 2020;6(8):e04603. doi: 10.1016/j.heliyon.2020.e04603.
[16] Bhat M, Ranjitha MT, Mamatha SV, Nayak R, Das R, Roymahapatra G. Removal of Congo red, patton reeder's, and rhodamine B dyes from aqueous solution using Tabebuiarosea Peel as natural adsorbent. ES Food Agrofor. 2024;16:1–9.
[17] Ren YS, Seilkhan A, Akbota B, Zhang S, Xu J, Khan H, et al. Treatment of dyes contaminated water using biochar derived from Eucalyptus wood waste. ES Mater Manuf. 2024;25:1236–46.
[18] Khun K. Synthesising metal oxide materials and their composite nanostructures for sensing and optoelectronic device applications. PhD diss., Linköping University Electronic Press; 2015.
[19] Comini E, Baratto C, Concina I, Faglia G, Falasconi M, Ferroni M, et al. Metal oxide nanoscience and nanotechnology for chemical sensors. Sens Actuators, B Chem. 2013;179:3–20.
[20] More SG, Pathan HM, Jadkar SR, Gadakh SR. Biomolecule-assisted hydrothermal synthesis of copper aluminium sulfide: application for dye degradation. ES Energy Env. 2024;25:1209–19.
[21] Nandanwar R, Bamne J, Singh N, Taiwade K, Chandel V, Sharma PK, et al. Synthesis of titania-silica nanocomposite for enhanced photodegradation of methylene blue and methyl orange dyes under UV and Mercury lights. ES Mater Manuf. 2022;16:78–88.
[22] Khanvilkar MB, Nikumbh AK, Pawar RA, Karale NJ, Nagwade PA, Nighot DV, et al. Effect of divalent/trivalent doping on structural, electrical and magnetic properties of spinel ferrite nanoparticles. Eng Sci. 2023;22:850–71.
[23] Dahivade PB, Pawar SN, Pathan HM, Lokhande BJ. Temperature-dependent hydrothermal synthesis of CdO nanoparticles and its analysis for supercapacitor application. ES Energy Env. 2024;24:1098–100.
[24] Lu J, Yang Y, Zhong Y, Hu Q, Qiu B. The study on activated carbon, magnetite, polyaniline and polypyrrole development of methane production improvement from wastewater treatment. ES Food Agrofor. 2022;10:30–8.
[25] Dahivade PB, Pawar SN, Lokhande BJ. Structural, morphological, and electrochemical analysis of electrodeposited iron oxide electrodes. ES Energy Env. 2023;20:1–7.
[26] Kamran M, Ali H, Saeed MF, Bakhat HF, Hassan Z, Tahir M, et al. Unraveling the toxic effects of iron oxide nanoparticles on nitrogen cycling through manure-soil-plant continuum. Ecotoxicol Env Saf. 2020;205:111099. doi: 10.1016/j.ecoenv.2020.111099.
[27] Kabdrakhmanova S, Joshy KS, Sathian A, Aryp K, Akatan K, Shaimardan E, et al. Anti-bacterial activity of Kalzhat Clay functionalized with Ag and Cu nanoparticles. Eng Sci. 2023;26:1–7.
[28] Alkhrissat T, Alqaraleh L, Kassab G, Abdel-Jaber M. Impact of iron oxide nanoparticles on anaerobic co-digestion of chicken manure and sewage sludge substrates. Eng Sci. 2024;30:1–13.
[29] Yarjanli Z, Ghaedi K, Esmaeili A, Rahgozar S, Zarrabi A. Iron oxide nanoparticles may damage to the neural tissue through iron accumulation, oxidative stress, and protein aggregation. BMC Neurosci. 2017;18(1):1–12.
[30] Nambiar NK, Brindha D, Punniyakotti P, Venkatraman BR, Angaiah S. Derris indica leaves extract as a green inhibitor for the corrosion of aluminium in alkaline medium. Eng Sci. 2022;17:167–75.
[31] Kashyp NK, Das AK, Bhardwaj AK, Roymahapatra G, Ghosh A, Hiat M, et al. Phytochemical Analysis of Careya arborea Roxb. Root Extracts: A Qualitative Analytical Approach. ES. Gen. 2023;1(4):959–66.
[32] Vatandost E, Chekin F, Shahidi Yasaghi SA. Green synthesis of silver nanoparticles by pepper extracts reduction and its electocatalytic and antibacterial activity. Russ J Electrochem. 2016;52(10):960–5.

[33] Sharif Nasirian V, Shahidi SA, Tahermansouri H, Chekin F. Application of graphene oxide in the adsorption and extraction of bioactive compounds from lemon peel. Food Sci Nutr. 2021;9(7):3852–62.
[34] Davarnia B, Shahidi SA, Karimi-Maleh H, Saraei AGH, Karimi F. Biosynthesis of Ag nanoparticle by peganum harmala extract; antimicrobial activity and ability for fabrication of quercetin food electrochemical sensor. Int J Electrochem Sci. 2020;15(3):2549–60. doi: 10.20964/2020.03.70.
[35] Tabrizi M, Shahidi SA, Chekin F, Ghorbani-HasanSaraei A, Raeisi SN. Reduce graphene oxide/Fe_3O_4 nanocomposite biosynthesized by sour lemon peel; using as electro-catalyst for fabrication of vanillin electrochemical sensor in food products analysis and anticancer activity. Top Catal. 2022;65:726–32.
[36] Hossain MA, Akhter S, Sohrab MH, Afroz F, Begum N, Rony SR. Applying an optimization technique for the extraction of antioxidant components from Justicia adhatoda leaves. Eng Sci. 2023;24:12–4.
[37] Rosli IR, Zulhaimi HI, Ibrahim SKM, Gopinath SCB, Kasim KF, Akmal HM, et al. Phytosynthesis of iron nanoparticle from Averrhoa Bilimbi Linn. IOP Conf Ser Mater Sci Eng. 2018;318(1):012012.
[38] Haris M, Fatima N, Iqbal J, Chalgham W, Mumtaz AS, El-Sheikh MA, et al. Oscillatoria limnetica mediated green synthesis of iron oxide (Fe_2O_3) nanoparticles and their diverse in vitro bioactivities. Molecules. 2023;28(5):2091–109.
[39] Harmansah C, Karatay Kutman M, Biber Muftuler FZ. Preparation of iron oxide nanoparticles by banana peels extract and its usage in NDT. Meas J Int Meas Confed. 2022;204:112081. doi: 10.1016/j.measurement.2022.112081.
[40] Harith SS, Yasim NH, Harun A, Omar WS, Musa MS. Phytochemical screening, antifungal and antibacterial activities of Musa acuminata plant. Malays J Anal Sci. 2018;22(3):452–7.
[41] Haq S, Afsar H, Ali MB, Almalki M, Albogami B, Hedfi A. Green synthesis and characterization of a ZnO–ZrO_2 heterojunction for environmental and biological applications. Crystals. 2021;11:1–12.
[42] Haq S, Rehman W, Waseem M, Rehman MU, Shah KH. Modeling, thermodynamic study and sorption mechanism of cadmium ions onto isopropyl alcohol mediated tin dioxide nanoparticles. J Inorg Organomet Polym Mater. 2020;30(4):1197–205.
[43] Haq S, Rehman W, Waseem M. Adsorption efficiency of anatase TiO_2 nanoparticles against cadmium ions. J Inorg Organomet Polym Mater. 2018;29(3):651–8.
[44] Rehman MU, Rehman W, Waseem M, Shah BA, Shakeel M, Haq S, et al. Fabrication of titanium-tin oxide nanocomposite with enhanced adsorption and antimicrobial applications. J Chem Eng Data. 2019 Jun;64(6):2436–44.
[45] Hafeez M, Zeb M, Khan A, Akram B, Abdin ZU, Haq S, et al. Populus ciliata mediated synthesis of silver nanoparticles and their antibacterial activity. Microsc Res Tech. 2021;84(3):480–8.
[46] Haq S, Rehman W, Waseem M, Javed R, Rehman MU, Shahid M. Effect of heating on the structural and optical properties of TiO_2 nanoparticles: antibacterial activity. Appl Nanosci. 2018;8:11–8.
[47] Askri D, Cunin V, Béal D, Berthier S, Chovelon B, Arnaud J, et al. Investigating the toxic effects induced by iron oxide nanoparticles on neuroblastoma cell line: an integrative study combining cytotoxic, genotoxic and proteomic tools. Nanotoxicology. 2019;13(8):1021–40. doi: 10.1080/17435390.2019.1621399.
[48] Pereira MS, Ribeiro TS, Lima FAS, Santos LPM, Silva CB, Freire PTC, et al. Synthesis and properties of Sn1−x$FexO_2$ nanoparticles obtained by a proteic sol–gel method. J Nanopart Res. 2018;20(8):212–22.
[49] Shah A, Tauseef I, Ali MB, Yameen MA, Mezni A, Hedfi A, et al. In-vitro and in-vivo tolerance and therapeutic investigations of phyto-fabricated iron oxide nanoparticles against selected pathogens. Toxics. 2021;9:105–20.
[50] Chen Z, Geng Z, Zhang Z, Ren L, Tao T, Yang R, et al. Synthesis of magnetic Fe_3O_4@C nanoparticles modified with $-SO_3H$ and −COOH groups for fast removal of Pb^{2+}, Hg^{2+}, and Cd^{2+} ions. Eur J Inorg Chem. 2014;2014(20):3172–7.
[51] Rendon JL, Serna CJ. IR spectra of powder hematite: effects of particle size and shape. Clay Min. 1981;16:375–81.
[52] Rehman FU, Mahmood R, Ali MB, Hedfi A, Mezni A, Haq S, et al. Physicochemical, photocatalytic, antibacterial, and antioxidant screening of bergenia ciliata mediated nickel oxide nanoparticles. Crystal. 2021;11:1137.
[53] Shoukat S, Rehman W, Haq S, Waseem M, Shah A. Synthesis and characterization of zinc stannate nanostructures for the adsorption of chromium (VI) ions and photo-degradation of rhodamine 6G. Mater Res Express. 2019;6(11):115052. doi: 10.1088/2053-1591/ab473c.
[54] Haq S, Shoukat S, Rehman W, Waseem M, Shah A. Green fabrication and physicochemical investigations of zinc-cobalt oxide nanocomposite for wastewater treatment. J Mol Liq. 2020;318:114260. doi: 10.1016/j.molliq.2020.114260.
[55] Bibi N, Haq S, Rehman W, Waseem M, Rehman MU, Shah A, et al. Low temperature fabrication of SnO_2, ZnO and Zn_2SnO_4 nanostructures for the degradation of Rhodamine 6G: characterization. Biointerface Res Appl Chem. 2020;10(4):5895–900.
[56] Haq S, Ali MB, Mezni A, Hedfi A, Rehman W, Waseem M, et al. Highly crystalline zinc stannate nanocatalyst for rhodamine 6G degradation: synthesis and characterization. J Ovonic Res. 2022;18(2):121–7.
[57] Haq S, Sarfraz A, Menaa F, Shahzad N, Din SU, Almukhlifi HA, et al. Green synthesis of NiO-SnO_2 nanocomposite and effect of calcination temperature on its physicochemical properties: impact on the photocatalytic degradation of methyl orange. Molecules. 2022;27(23):1–19.
[58] Haq S, Afsar H, Din IU, Ahmad P, Khandaker MU, Osman H, et al. Enhanced photocatalytic activity of ficus elastica mediated zinc oxide-zirconium dioxide nanocatalyst at elevated calcination temperature: Physicochemical study. Catalysts. 2021;11(12):1–15.
[59] Zada N, Saeed K, Khan I. Decolorization of Rhodamine B dye by using multiwalled carbon nanotubes/Co–Ti oxides nanocomposite and Co–Ti oxides as photocatalysts. Appl Water Sci. 2020;10(1):1–10.
[60] Yuan H, Xu J. Preparation, characterization and photocatalytic activity of nanometer SnO_2. Appl Catal B Env. 2010;1(3):269–79.
[61] Haq S, Ehsan R, Menaa F, Shahzad N, Din SU, Shahzad MI, et al. A novel shift in the absorbance maxima of methyl orange with calcination temperature of green tin dioxide nanoparticle-induced photocatalytic activity. Catalysts. 2022;12(11):1397–403.
[62] Kaur J, Bansal S, Singhal S. Photocatalytic degradation of methyl orange using ZnO nanopowders synthesized via thermal decomposition of oxalate precursor method. Phys B Condens Matter. 2013;416:33–8. doi: 10.1016/j.physb.2013.02.005.
[63] Helmiyati H, Fitriana N, Chaerani ML, Dini FW. Green hybrid photocatalyst containing cellulose and γ–Fe_2O_3–ZrO_2 heterojunction for improved visible-light driven degradation of Congo red. Opt Mater (Amst). 2022;124:111982.
[64] Hammad EN, Salem SS, Mohamed AA, El-Dougdoug W. Environmental impacts of ecofriendly iron oxide nanoparticles on dyes removal and antibacterial activity. Appl Biochem Biotechnol. 2022;194(12):6053–67. doi: 10.1007/s12010-022-04105-1.